Chapter 17

Functional Imaging Using Fluorine (^{19}F) MR Methods: Basic Concepts

Sonia Waiczies, Christian Prinz, Ludger Starke, Jason M. Millward, Paula Ramos Delgado, Jens Rosenberg, Marc Nazaré, Helmar Waiczies, Andreas Pohlmann, and Thoralf Niendorf

Abstract

Kidney-associated pathologies would greatly benefit from noninvasive and robust methods that can objectively quantify changes in renal function. In the past years there has been a growing incentive to develop new applications for fluorine (^{19}F) MRI in biomedical research to study functional changes during disease states. ^{19}F MRI represents an instrumental tool for the quantification of exogenous ^{19}F substances in vivo. One of the major benefits of ^{19}F MRI is that fluorine in its organic form is absent in eukaryotic cells. Therefore, the introduction of exogenous ^{19}F signals in vivo will yield background-free images, thus providing highly selective detection with absolute specificity in vivo. Here we introduce the concept of ^{19}F MRI, describe existing challenges, especially those pertaining to signal sensitivity, and give an overview of preclinical applications to illustrate the utility and applicability of this technique for measuring renal function in animal models.

This chapter is based upon work from the COST Action PARENCHIMA, a community-driven network funded by the European Cooperation in Science and Technology (COST) program of the European Union, which aims to improve the reproducibility and standardization of renal MRI biomarkers. This introduction chapter is complemented by two separate chapters describing the experimental procedure and data analysis.

Key words Magnetic resonance imaging (MRI), Fluorine (^{19}F), Kidney, Inflammation, Tissue oxygenation

1 Introduction

The need for methods to assess renal function that are both robust and noninvasive is increasingly becoming recognized. One approach is to use MRI in combination with contrast agents that are responsive to physiological changes [1]. The most common type of MR contrast agents are paramagnetic agents that enhance contrast on MR images. These contrast agents act by modulating proton (^{1}H) relaxation, either during recovery (T_1 component) or

Andreas Pohlmann and Thoralf Niendorf (eds.), *Preclinical MRI of the Kidney: Methods and Protocols*, Methods in Molecular Biology, vol. 2216, https://doi.org/10.1007/978-1-0716-0978-1_17, © The Author(s) 2021

decay (T_2 component) of the MR signal. In order for a contrast agent to be useful to identify changes in a specific physiological phenomenon, its sensitivity to detect and quantify physiological changes on MRI and its pharmacokinetic properties must be balanced [2].

From a technical point of view, paramagnetic contrast agents have a concomitant effect on all components of MR relaxation; the interplay between T_1 and T_2 relaxation depends on the dose and location of the contrast agent as well as the MR imaging sequence used [3]. This complexity is exacerbated by intrinsic factors such as deoxygenated blood or air cavities that may confound the signal being investigated [4]. A case in point is when imaging cells labeled with contrast agent: changes in contrast created by such intrinsic tissue factors could render the labeled cells indistinguishable from the surrounding tissue. This drawback is heightened by the signal sensitivity constraints due to the low concentrations of contrast agent (<μM range). As a result, any quantification of the physiological observation is hampered, and in some cases, no definitive conclusions can be made.

The use of fluorinated agents in combination with fluorine (^{19}F) MRI overcomes the hurdle of signal ambiguity because the ^{19}F MR signal is specific to the administered ^{19}F agent. While the ^{19}F nucleus has similar MR sensitivity and resonance frequency as ^{1}H, unlike ^{1}H, it is practically absent in vivo, that is, there are no endogenous ^{19}F organic forms in vivo. Therefore, any exogenous fluorinated compounds introduced in vivo can be detected with high selectivity and absolute specificity. This has been exploited to noninvasively track cells in vivo using ^{19}F MRI after labeling them with ^{19}F compounds, typically in the form of nanoparticles (NP). Interestingly, the chemical shift range for ^{19}F is much larger than that of ^{1}H. Organofluorine compounds span a chemical shift range of over 350 ppm [5]. Thus multiple ^{19}F nuclei resonances for organofluorine compounds can be easily separated, even under rather inhomogeneous conditions [6]. The unique properties of ^{19}F nuclei as well as ^{19}F compounds have been the driving force behind the increasing interest in ^{19}F MRI. However, the application of ^{19}F MRI to a wide range of biomedical research fields has been restricted by the low abundance of ^{19}F nuclei in vivo following exogenous administration. This constraint is compounded by the fact that the signal sensitivity of current MR hardware remains limited, making the detection of ^{19}F compounds present at low concentrations extremely challenging. Therefore, one strategy in ^{19}F MRI to circumvent this is to boost the signal-to-noise ratio (SNR) as a function of time, that is, the SNR efficiency to enhance signal sensitivity and improve detection limits.

From a biological perspective, several key components must be considered when using contrast agents to study renal function. Among other physicochemical properties, size will determine the pharmacokinetic properties of the contrast agent as well as its uptake

by cells in vivo. For example, low-molecular-weight-gadolinium-based contrast agents (GBCAs) are filtered through the glomerulus and are not reabsorbed by the renal tubule. Conversely, larger contrast agents such as paramagnetic iron oxide particles or ^{19}F nanoparticles commonly follow a one-compartment pharmacokinetic model within the blood [7]. These nanoparticles are too large to be filtered by the glomerulus and are eventually taken up by phagocytic blood cells. Such nanoparticles including the iron replacement therapy ferumoxytol have a long intravascular half-life (>14 h) and are therefore useful for vascular and perfusion-weighted MRI [8]. Unless inflammatory processes are ongoing, these particles will localize primarily in the liver and will eventually undergo elimination via hepatic clearance. The clearance of nanoparticles via liver or kidney is dependent on their size and surface properties [9] but also on the health status of these organs, such that clearance should be critically studied [10] especially prior to patient studies.

This introduction chapter is complemented by two separate chapters describing the experimental procedure and data analysis, which are part of this book.

This chapter is part of the book Pohlmann A, Niendorf T (eds) (2020) Preclinical MRI of the Kidney—Methods and Protocols. Springer, New York.

2 Overview of Applications

Quantitative measurements of renal function are necessary to detect changes already during the early stages of kidney disease, to support disease staging and to screen emerging therapeutic strategies. Non-invasive and rapid MR methods are needed to quantify disease components such as inflammation, hypoxia and tissue damage. While commonly available MR contrast agents act by modulating ^{1}H relaxation, contrast agents containing ^{19}F have also been developed to investigate disease components such as inflammation and to quantify pathological changes in the tissue microenvironment (e.g., changes in tissue oxygenation (pO_2) or pH) using ^{19}F MRI.

2.1 ^{19}F MRI to Study Environmental Changes in the Kidney In Vivo

There is an abundant repertoire of exogenous MRI contrast agents that act by modulating ^{1}H relaxation and which are triggered by changes in pO_2, pH or temperature as well as changes in protein, metabolite or metal ion concentrations (reviewed elsewhere [1]). Here we focus on the application of ^{19}F probes that elicit a desired MR signal following changes in pO_2 and pH and hold promise as tools for screening kidney disease.

2.1.1 Renal Tissue Oxygenation

Healthy kidneys operate under relatively low O_2 conditions, requiring extensive extraction of O_2 from flowing blood. While several regulatory mechanisms act to maintain oxygenation within homeostatic limits, the kidneys are nonetheless particularly susceptible to

hypoxic injury [11]. While O_2 consumption determines perfusion in most nonrenal tissue such as the brain, perfusion determines O_2 consumption in the kidney [12]. Therefore, a sudden temporary impairment of the blood flow to the kidney results in acute kidney injury (AKI) as a result of impaired O_2 delivery. Approaches for identifying and treating AKI as early as possible should aim at detecting and restoring imbalances the homeostasis between renal oxygenation and factors such as nitric oxide that control the renal microcirculation [13].

Noninvasive methods to measure kidney function in vivo, specifically tissue pO_2 and blood perfusion, are crucial. Arterial spin labeling MRI determines intrarenal perfusion without the need of exogenous contrast agents, and will be reviewed in a separate chapter of this book. MRI techniques that utilize the native ^{1}H contrast from blood—blood-oxygenation-level-dependent (BOLD) MRI—have been proposed [14]. The level of renal oxygenation within each voxel is quantified by mapping the shortening of ^{1}H T_2^* induced by deoxyhemoglobin—deoxyHb [15]. However, the relation of T_2^* to tissue pO_2 may be confounded by factors such as hematocrit, oxyHb dissociation curve, and the vascular volume fraction. This underscores the need for careful scrutiny of this relation in order to make quantitative interpretations [16].

Perfluorocarbon (PFC) emulsions offer an alternative to quantify changes in tissue pO_2 during vascular pathology [17, 18]. More recently PFC NPs were also employed as a theranostic strategy for studying perfusion and treating AKI [19]. Primarily PFC NPs have been used to assess perfusion in the renal microvasculature following AKI [20]. ^{19}F MRI sensitively detected decreased RBV and pO2 in the cortical–medullary (CM) junction 24 h following unilateral (left) renal ischemia–reperfusion [20], where increased T_2^* was also observed by ^{1}H BOLD MRI (Fig. 1a). The T_2^*, ^{19}F signal, and pO_2 in the renal cortex of injured kidneys were all comparable to the contralateral control kidney, suggesting recovery of perfusion and oxygenation in this region. In the inner medulla, however, vascular leakage and hemorrhage-induced extravascular retention of PFC NPs (Fig. 1b, c) resulted in a false readout of reduced ^{1}H T_2^*, increased ^{19}F signal intensity, and unchanged pO2.

PFCs and oxygen exhibit similarly low cohesive energy densities, such that both require little energy for mutual solubility [21]. The high oxygen-dissolving capacity of PFC emulsions makes them ideal as O_2 carriers. PFCs were, in fact, considered as artificial blood substitutes [22]. Fluosol-DA—a mixture of perfluorodecalin (PFD) and perfluorotributylamine—was the first PFC emulsion studied in humans in a trial of Japanese patients [23]. It was soon recalled due to its rather low oxygen transport capacity compared to that of red blood cells [24]. PFCs ultimately failed as blood substitutes (even as next generation products

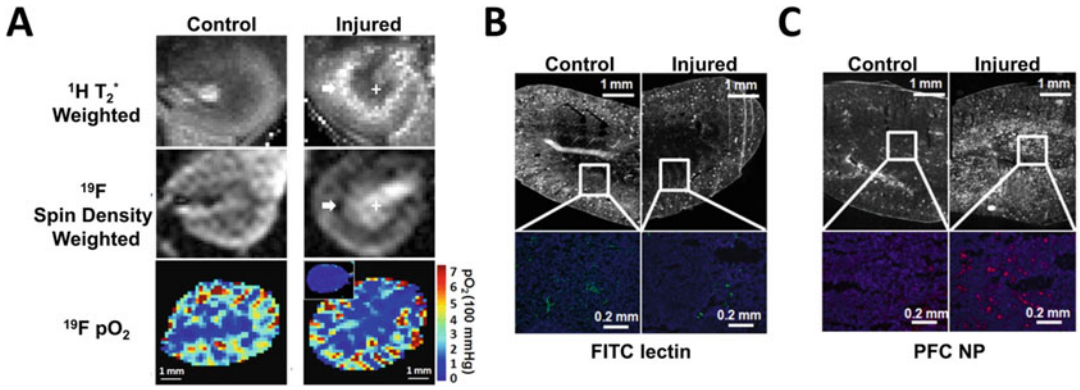

Fig. 1 Assessing perfusion in the renal microvasculature following acute kidney injury using PFCs. (**a**) Composite Representative ^{1}H T2*-weighted image (top row), ^{19}F spin density weighted image (middle row), and pO_2 map (bottom row) in the left control and right injured kidneys of the same mouse. (**b**) Fluorescence images showing FITC-lectin labeled perfused blood vessels in control and injured kidneys (top row) and zoom-in view of FITC-lectin (green) labeled perfused vessels in the CM junction (bottom row). (**c**) Fluorescence images showing rhodamine labeled PFC NPs in injured and control kidneys (top row) and zoom-in view showing PFC NPs (red) in the renal medulla (bottom row). Adapted from Hu L. et al. (2013) [20] with permission from John Wiley & Sons Inc.

appeared in the clinic). Although O_2-deprived tissues easily extract O_2 in PFCs, the oxygen dissociation curve of PFC emulsions is linear and monotonic, in contrast to the sigmoidal hemoglobin dissociation curve. Therefore, most of the O_2 dissolved in PFCs is released at high O_2 partial pressure in the arteries, with little O_2 being available for the capillaries where O_2 partial pressure is low but needed the most [22]. Interestingly Fluosol-DA (the first PFC that was used in patients [23]) was also used to acquire the first ^{19}F MR images in vivo, showing its accumulation in the rat liver [25]. The PFC in this emulsion gives complex MR spectra and has since been replaced by other PFCs with better imaging properties [26].

The longitudinal relaxation rate ($1/T_1$) of ^{19}F in PFCs was shown to depend linearly on O_2 partial pressure [27]. This led to the first noninvasive in vivo tissue O_2 assessments in tumor tissue and liver [28] and later in myocardial tissue [29]. The latter study provided the first proof of concept study for rapid, noninvasive measurements of O_2 oxygen tension changes in response to ischemia and reperfusion [29]. It is claimed that the size of PFC nanoparticles (>100 nm) confers upon them a good safety profile without renal toxicity, since they are not expected to be cleared through glomerular filtration. Therefore, unlike other imaging agents that undergo renal clearance (e.g., iodinated CT compounds, gadolinium MRI chelates), PFC emulsions do not increase the workload of the kidney and are not immediately considered as nephrotoxic [10].

2.1.2 Acid–Base Homeostasis in the Kidney and pH Sensors

The kidney plays a major role in acid–base homeostasis; this balance depends on its capacity to reabsorb filtered bicarbonate, mainly from the proximal tubule, and to excrete an equivalent amount of protons at the distal tubule [30]. CEST MRI was originally developed to measure pH with exogenous pH-responsive MRI contrast agents [31]. The pH in the kidney following AKI gradually increased from 6.7 to 7.2 as measured with CEST-MRI pH-responsive probes [32]. A major drawback of paramagnetic probes is that signal intensity is not only proportional to the pH but also to contrast agent concentration. Particularly in tumors, in vivo pH mapping assumes a constant contrast agent concentration across tissue notwithstanding poor perfusion where acidolysis occurs [33].

Approaches such as ratiometric $^{19}F/^{1}H$ probes have been developed to overcome the issue of quantification; the signal is normalized to the concentration of the contrast agent by means of a concentration reporting (^{19}F) moiety [34]. Another advantage of ^{19}F MR probes is the larger range in chemical shifts in ^{19}F (compared to ^{1}H). These chemical shifts are highly sensitive to the immediate surroundings, such that small chemical changes can lead to dramatic changes in chemical shift [6]. The first ^{19}F MR probe identified as a candidate to probe cellular pH was the vitamin B6 analog 6-fluoropyridoxol (6-FPOL) reported to have a pK_a in the physiological range and large chemical shift response [35]. Subsequently the feasibility of using 6-FPOL to probe cellular pH was demonstrated in whole blood [36]. The concept of employing ^{19}F MR probes for in vivo imaging was introduced when a series of fluorinated vitamin B6 analogs with a chemical shift sensitivity in the range 7.4–12 ppm were synthesized as pH indicators [37]. The sensitivity of ^{19}F MRS probes can be further improved by incorporating paramagnetic metal ions that further amplify the chemical shift between protonated and deprotonated forms by the presence of covalent and dipolar contributions [38, 39]. Iron (II) complexes were also explored to exploit the pH-dependent spin-state population change; the ^{19}F NMR chemical shift was in a sensitivity range of 13.9 ppm per pH unit at 37 °C [40]. More recently fluorinated nickel (II) complexes with diamagnetic and paramagnetic properties were designed for ratiometric pH mapping by ^{19}F MRI [41]. Supramolecular nanostructures formed by fluorinated peptide amphiphiles transitioning from cylindrical to ribbon-like shape as pH increases from 4.5 to 8.0 resulting in enhanced MR signals. These nanostructures represent a good strategy to design stimulus-responsive ^{19}F MRI contrast agents for responses to pH changes in vivo [42].

2.2 ^{19}F MRI to Study Renal Inflammation In Vivo

Together with renal tissue hypoxia and tubular injury, inflammation is one underlying component in the pathology of AKI [43]. Studies suggest that systemic inflammation causes ischemic injury in one organ and that repercussions follow in distant organs downstream

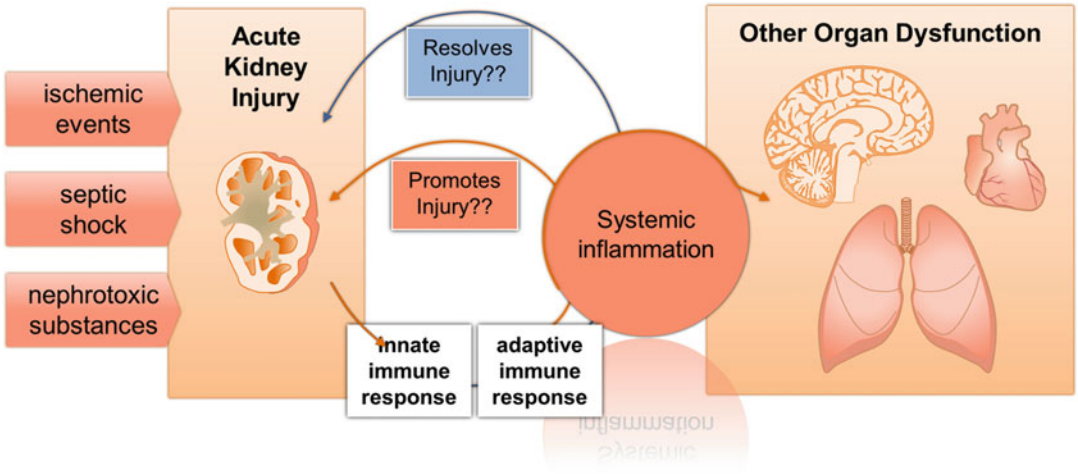

Fig. 2 Inflammation as one underlying factor in the pathology of AKI. AKI can be triggered by a variety of clinical disorders ranging from renal ischemic events to sepsis and exposure to nephrotoxic substances. The kidney is tightly connected with the interior milieu of the body such that even the slightest of changes will be rapidly detected and communicated between the kidney and the rest of the body

of the ischemic event [44–46] (Fig. 2). Therefore, methods that can non-invasively quantify the level of inflammation in different organs would be crucial to identify the causality and significance of inflammation during both systemic and kidney-specific disease.

^{19}F MRI is commonly used in association with an intravenous administration of PFC emulsions to study the distribution of inflammatory cells in vivo [26, 47–51]. ^{19}F MRI is performed after an in vivo labeling of inflammatory cells with a ^{19}F compound—typically in nanoparticle (NP) form. The ^{19}F-NPs are administered intravenously in order for them to be taken up by inflammatory cells that are migrating through the systemic circulation into inflamed organs. Typically, PFCs such as perfluoro-15-crown-5 ether (PFCE) are used to prepare NPs for cell labeling. PFCE is biologically stable and provides a high payload of ^{19}F nuclei since it contains 20 chemically equivalent ^{19}F spins.

In a rat model of orthotopic kidney transplantation, ^{19}F MRI was used to study inflammation in the kidney undergoing rejection [48]. Three days following transplantation, PFCE NPs were administered intravenously and ^{1}H/^{19}F images acquired 2 and 24 h following NP infusion (Fig. 3a). At the earlier time point, the ^{19}F signal was mainly found in the circulation but also in small but roughly equal amounts in both the native and transplanted kidneys (Fig. 3a). By day 4 posttransplantation (i.e., 24 h following PFCE NP), the transplanted kidney underwent moderate (Grade 2) rejection and showed an intense signal in the allograft kidney and in liver and spleen, but the ^{19}F signal was virtually undetectable above the level of image noise in the native kidney (Fig. 3a). T_2*-weighted

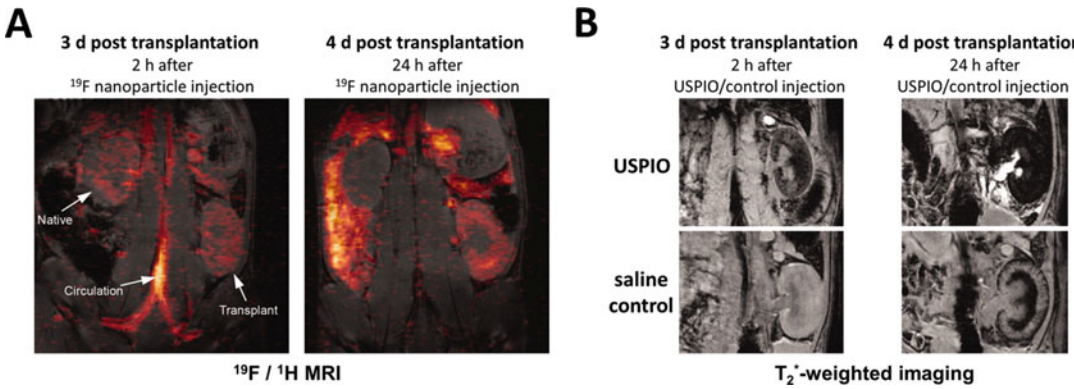

Fig. 3 Inflammation in the kidney in a rat model of orthotopic kidney transplantation experiencing rejection. (**a**) Composite $^{1}H/^{19}F$ images of an orthotopic kidney transplant recipient ~2 h post–PCE injection on POD 3 with ^{19}F signal found in the vasculature and equally in both the native (upper) and graft (lower) kidneys (left) and ~24 h post–PCE injection with ^{19}F signal in the allograft kidney, as well as other organs (right). (**b**) Allograft kidney on POD 4 following an injection (left) of 6 mg/kg BW USPIO (upper row) or following an injection of saline (lower row) and 24 h later (right). Adapted from Hitchens T.K. et al. (2011) [48] with permission from John Wiley & Sons Inc.

imaging reveals hemorrhaging in the medulla on day 4 post-kidney transplantation, which can be detected both in animals administered ultrasmall superparamagnetic iron oxide (USPIO) NPs but also in transplants without USPIO (saline control) (Fig. 3b). This can confound the detection of USPIO-labeled macrophages and exhibits one of the advantages of ^{19}F MRI over iron oxide-based NPs.

Apart from labeling inflammatory cells in vivo, NPs have been used to label specific immune cell types such as dendritic cells (DCs) ex vivo, prior to their administration in vivo [52–54]. This kind of labeling is particularly useful to label cellular therapies that will be administered in patients as part of a treatment strategy [55]. In addition to cancer patients, kidney transplantation patients would also benefit from cell-based therapies, specifically the types of cells inducing tolerance [56]. Monocyte-derived suppressor cell products are currently being investigated alongside immunosuppressive therapies in kidney transplant recipients with promising results [57]. These candidate therapies would benefit from a labeling strategy that will enable them to be tracked in vivo over time with ^{19}F MRI. The possibility of quantifying the ^{19}F MR signal would allow an objective assessment of the spatial and temporal cellular distribution within the same individual. This kind of labeling and ^{19}F MRI would result in absolute cell quantification, since the ^{19}F MR signal is generated from the cells alone, by direct detection of the ^{19}F spins in the cells labeled with ^{19}F NPs, without any confounding background MR signal. However, several biological and technical considerations need to be made, in order to achieve a truly absolute MR signal quantification: not all cell types can be labeled with the ^{19}F NPs currently available (Subheading 3.1.1).

3 Basic Concepts of ^{19}F MRI

3.1 ^{19}F imaging Probes

The design and synthesis of novel fluorine-rich molecular labels and imaging probes is an important domain for ^{19}F MRI. For several years, a wide range of fluorine probes has been available for experimental and even clinical applications [58, 59].

3.1.1 ^{19}F Probes for Cellular Uptake

Current procedures used to label cells with nanoparticles take advantage of the intrinsic nature of cells to engulf foreign bodies, a cellular property known as phagocytosis. Dendritic cells are intrinsically phagocytic and therefore ideal candidates for tracking with ^{19}F MRI [52, 53, 55, 60–62]. Cells labeled with clinical grade ^{19}F nanoparticles have been administered as immunotherapies in cancer patients [55]. This tracking method could support several other cell therapy studies, including those dealing with kidney transplantation [63].

Enhancing cellular uptake is desirable, even for cells that are intrinsically phagocytic. Several studies have investigated the incorporation of phosphatidylserine (PS) in nanoparticle-based therapeutics to enhance their uptake [64]. After renal ischemia–reperfusion, the signal from PS-containing microbubbles was two-fold higher than that for standard lipid microbubbles [65]. Phospholipids such as PS and phosphatidylethanolamine (PE) are important components of biological cell membranes and are important components for endocytosis in phagocytic cells such as DCs [66]. We previously reported that enrichment of ^{19}F nanoparticles with 1,2-dipalmitoyl-sn-glycero-3-PE (DPPE) resulted in a striking increase (at least one order of magnitude) in cytoplasmic uptake in DCs [62]. Interestingly, membrane lipid-raft processes have been proposed as trafficking mechanisms for transporting therapeutic cargo such as siRNA [67] or targeting ligands [68] into the cytoplasm, circumventing the usual endosomal uptake pathway.

Labeling cells with low intrinsic phagocytic properties (such as T cells) will prove more difficult using the above strategy, even if the nanoparticle size is lower than 180 nm [69]. Some research groups claim to have labeled T cells using the same above principles [70]. T cells are not able to internalize nanoparticles, even small iron oxide nanoparticles (core diameter = 12.5 nm), as has been clearly shown by transmission electron microscopy (TEM), considered to be a definitive method, and also by confocal microscopy [71]. For the latter method nanoparticles with fluorescent tags were used to corroborate the in vivo ^{19}F signals with ex vivo fluorescence microscopy signals, but the authors also included a cell membrane stain [71]. This is a necessary control to distinguish membrane association from intracellular distribution, in light of the point spread function contribution [72]. Another key point is that the fluorescent tag dissociates from the fluorine label over time, both in vitro and in vivo [73]. This has a critical impact on the interpretation of long-term experiments validated by standard fluorescent techniques.

Before taking the next steps toward administering cells in vivo, it is essential to understand how nanoparticles are recognized, internalized, trafficked, and distributed within the specific host cell [74]. This is critical when contemplating labeling of cells that may ultimately be applied in vivo to patients in a therapeutic context. Cells that are not intrinsically phagocytic will not readily internalize NPs but might still exhibit a ^{19}F MR signal ex vivo, due to reasons such as transitional binding of NPs to the cell membrane or incomplete clearing of noninternalized NPs from the cell culture medium. The ^{19}F MR signals following administration of ineffectively labeled cells with contaminating NPs would be misrepresentative of the actual distribution of the cells in vivo. Therefore, we need to ask the right questions regarding the specific cell type to be labeled, and the methods used prior to transfer of the cells into living organisms [75].

3.1.2 ^{19}F Probes with Increased Signal Sensitivity

Fluorinated probes are commonly designed with the goal of improving signal strength by increasing the number of fluorine atoms per molecule [59]. Linear ^{19}F polymers such as perfluoropolyethers (PFPEs) are the simplest choice to achieve increased fluorine content but the NPs produced with these polymers are polydisperse and the presence of multiple chemical shifts presents several peaks in the ^{19}F spectra [76]. Superfluorinated branched ^{19}F probes such as ^{19}FIT [77] and PERFECTA [78] promise several advantages, specifically a very high fluorine nuclei density with a single ^{19}F spectral peak. These probes therefore afford enhanced sensitivity and better imaging performance than linear perfluoropolymers. Unlike PERFECTA [78], the bispherical fluorocarbon ^{19}FIT is water soluble [77] and therefore possesses low organ retention, but it cannot be emulsified into nanoparticles for cell labeling strategies. Increasing the density of ^{19}F nuclei can only go so far in terms of increased sensitivity of ^{19}F probes. Ultimately, a limit to this density will be reached.

Another strategy to promote ^{19}F MR signal is to manipulate the MR properties of the ^{19}F probes in order to favor ideal conditions for MR signal acquisition. One approach is to decrease the T_1 of the ^{19}F nuclei, which is typically in the range of 0.5–3 s for diamagnetic compounds. Paramagnetic metal ions such as lanthanides(III) or iron(II) reduce the T_1 of ^{19}F compounds [38]. Paramagnetic centers affect the relaxation of ^{19}F nuclei (paramagnetic relaxation enhancement or PRE effect) via a number of mechanisms, most notably electron–nucleus dipole–dipole interaction and Curie relaxation [39], both of which are influenced by the effective magnetic moment (μ_{eff}) of the paramagnetic metal [79]. Other than the μ_{eff} of the metal ion, the PRE effect is also influenced by the distance separating the ^{19}F nuclei and the paramagnetic metal ion [39]. While long distances will severely diminish PRE, short

distances will substantially shorten the spin–spin relaxation time T_2. Thus T_1 reduction by molecular design should be dealt with carefully since it could also lead to a reduction in the T_2 and thereby line broadening of the resonance, which ultimately affects sensitivity [80]. The most sensitive metal-based probes are, in fact, not those whose metal ions have the highest μ_{eff}, but rather those who have the ideal distance separating ^{19}F from the paramagnetic metal ion (4.5–7.5 Å) thus resulting in higher T_2/T_1 ratios [81]. Nonetheless even at larger ^{19}F–M distances (>10 Å), the PRE effect can still be notable as is the case for a DOTA-based ^{19}F chelator [82]. In paramagnetic PFC nanoparticles, the ^{19}F MR relaxation enhancement has also been explained by diffusion mechanisms attributed to the changes in Brownian motion of PFC molecules inside the NP in conjunction with their ability to permeate into the lipid surfactant coating [83].

Introduction of paramagnetic metals in the design of ^{19}F probes not only results in a decrease T_1 of ^{19}F nuclei but also leads to paramagnetic induced chemical shifts. The CEST signal generated by paramagnetic involvement (PARACEST) will also be modulated by pH (Subheading 2.1.2). A macrocyclic Fe (II) complex bearing both exchangeable ^{1}H and ^{19}F was shown to behave as a ratiometric pH-responsive MRI contrast agent, whereby the CEST, but not the ^{19}F MR signal was pH-dependent [84]. This enables accurate pH mapping without the use of multiple probes. More recently a DOTA macrocyclic structure complexed with Ni(II) metal was shown to exhibit larger separations between the ^{1}H CEST signal and water [85]. Though the in vivo application of ^{19}F PARACEST probes remains to be investigated, the available complexes will likely provide valuable information in the near future when probing pH changes in vivo.

3.2 MR Data Acquisition

3.2.1 Pulse Sequence Optimization

One way of improving signal sensitivity is to avoid signal losses such as those occurring during spin relaxation. Most fluorinated compounds generally have long T_1 relaxation times, which effectively increases the acquisition time. Together with the fact that there is a large range of relaxation times for ^{19}F MR, this motivates more reliable optimization of pulse sequences that is informed by the MR properties of the ^{19}F compounds under investigation. Sequence performance is largely dependent on the relaxation times of the addressed spin system but also on the conditions the nuclei are in, such as tissue oxygenation level [17].

The choice of the best pulse sequence and acquisition method is dictated by the MR properties, particularly the relaxation times, of the nuclei being measured. The acquisition protocol for each sequence should be optimized by tailoring detection schemes to the properties of the nucleus—also in relation to its environment—using relationships empirically drawn from simulations [86]. Relaxation times determine the time frames of signal losses, so the time

orchestration for data acquisition should be assigned correctly. Other parameters, such as acquisition bandwidths, should also be properly planned to avoid recording unnecessary noise and to achieve the highest possible SNR [87].

A number of ^{19}F MR studies using different pulse sequences have aimed to optimize the acquisition method to promote SNR efficiency and signal sensitivity [17, 87–90]. A large proportion of ^{19}F MR studies, especially those applying perfluorocarbons (PFCs) in vivo, have employed the turbo spin echo (SE) rapid acquisition using relaxation enhancement (RARE) sequence [26, 47, 50, 51, 91]. This method reduces acquisition time by accumulating multiple echoes (dictated by the turbo factor) within a single repetition time [92]. Optimal settings for echo train lengths and repetition time (TR) according to measured relaxation times (T_1/T_2 combinations) were calculated for RARE to improve sensitivity thresholds [90].

Although RARE is commonly been for studying PFCs in vivo, other sequences will be better suited for ^{19}F compounds that unlike typical PFCs have short T_2 relaxation times. In such cases signal detection might be technically challenging and will demand acquisition strategies properly adapted for the compound and its environment. Gradient echo (GE) sequences were used to maximize SNR efficiency for imaging paramagnetic macrocyclic ^{19}F molecules complexed to lanthanides [87]. These molecules exhibit T_1 values in the order of 1–15 ms and T_2* values in the order of 0.4–12 ms [88]. In the latter study a radial zero echo time (ZTE) sequence yielded a sensitivity gain of 27-fold when compared to nonparamagnetic molecules, while the GE sequence yielded a gain of 11-fold [88]. Additionally, the highest SNR efficiency gain was achieved when T_2/T_1 were close to 1, particularly for the ZTE pulse sequence, and when T_1 was in the range of 1–5 ms [88]. Even ^{19}F molecules with unique spectral properties will require a more individualized adjustment of the MR parameters; such molecules might benefit from sequences such as ultrashort echo time (UTE) that acquire signal before the spins dephase, taking into consideration destructive phase interference [93]. An efficient k-space sampling strategy will be necessary to achieve maximal SNR and artifact-free MR images [94]. To image perfluorooctyl bromide (PFOB) that has a rich spectrum with large chemical shifts, a radial UTE with a balanced steady-state free precession (bSSFP) pulse sequence showed superiority above other sequences, such as SE, GE, or bSSFP with Cartesian sampling [89]. However, radial sampling might not always be viable since k space sampling pattern effects need to be considered, which might altogether result in reduced SNR efficiency [86]. Another way to speed up data acquisition is synchronous multinuclear imaging. For this, the MR system needs to have the architecture suited to acquire images from more than one nucleus in a single pulse sequence [95]. Simultaneous proton

and ^{19}F MRI was performed in a preclinical model using a clinical MR scanner at 3 T [95].

3.3 Hardware Considerations

The similarity between ^{19}F and ^{1}H MR properties with respect to sensitivity and resonance frequency is an advantage, from an engineering perspective since similar pulse power settings can be used, and dual-tuned radio frequency (RF) coils for ^{19}F and ^{1}H MRI are more convenient to design [50, 96]. One way of improving the ^{19}F MR signal in vivo is to increase SNR by improving the sensitivity of the measuring instrument. Two hardware strategies to improve sensitivity for ^{19}F MR are to increase the strength of the static magnetic field (B_0), and to increase the sensitivity of the RF coil by cryogenic cooling.

3.3.1 Cryogenic Cooling

The sensitivity of the RF coil is an important factor limiting SNR and thereby the level of spatial and temporal resolution that is targeted for ^{19}F MRI [97]. Even when employing an RF coil with a homogeneous transmit field (B_1^+) distribution and dedicated for brain ^{19}F and ^{1}H MRI, the spatial resolution of in vivo ^{19}F MRI was limited to approximately 600 μm [50]. This level of spatial resolution prohibits a detailed understanding of inflammation dynamics. To overcome the sensitivity constraints in ^{19}F MR and improve detail of inflammatory cell location, we applied the concept of cryogenically cooling RF coil hardware to improve SNR by reducing thermal noise [98–100]. The cryogenically cooled RF coil (CryoProbe™) technology is commercially available for small animal MRI of ^{1}H and X-nuclei such as carbon (^{13}C) and phosphorous (^{31}P). For these X-nuclei this technology is expected to be particularly useful for increasing SNR. A gain in SNR of 3.0- to 3.5-fold was reported for the ^{13}C CryoProbe [101]. We recently compared a ^{19}F CryoProbe with a room temperature ^{19}F RF coil of similar size and reported on a maximal SNR gain of 15-fold and were able to study inflammation at an isotropic resolution of 150 μm [100].

Surface RF coils provide a very high SNR close to the region where they are applied. However, a decrease in signal amplitude with increasing distance from their surface is inherent to the geometry of their design. Inhomogeneities in the transmit (B_1^+) field cause a spatially varying flip angle (FA) and as a result signal quantification is hampered. Likewise, the receive (B_1^-) field of surface RF coils is position-dependent [102]. In the particular case of the ^{19}F CryoProbe, we observed a strong FA decrease with increasing distance from the surface of the coil [100]. Using a receive-only surface RF coil in combination with a volume resonator used for transmission would overcome B_1^+ inhomogeneities. With this configuration the transmitted FAs will be homogeneous, thus enabling quantification [103]. This option is not available when using CryoProbes, since they are typically built in the form of transceive (transmit–receive) RF coils with no active decoupling.

Particularly for quantitative ^{19}F MRI, a correction of the B_1^+ inhomogeneity will be necessary when comparing concentrations of PFC in vivo with an external standard of known ^{19}F concentration. Differences in the B_1^+ field between the region of interest in vivo and the external standard will result in errors when quantifying in vivo ^{19}F signals. Several approaches have been implemented to correct B_1^+ inhomogeneities retrospectively, even for ^{19}F MRI [104, 105]. These approaches typically include RF pulse sequences for which an analytical knowledge of the signal intensity dependency on the FA exists.

3.3.2 Magnetic Field Strengths

Increasing the strength of the static magnetic field (B_0) will increase SNR of the measured signal [106], a strategy which is actively being pursued for clinical application [107]. Intrinsic SNR is expected to grow at least linearly with increasing B_0 strengths [97, 108, 109]. The principle of reciprocity can be used at low field strengths to calculate the receive field (B_1) sensitivity of a single channel RF coil in terms of the transmit field (B_1^+) that can be easily measured [110]. In studies performed at frequency (f) <1 MHz the maximum sensitivity was calculated to be proportional to the f: sensitivity $\propto f1.75$ [97, 108]. When going to higher magnetic field strengths, the increasing f and the influence of wave propagation need to be considered [106]. The homogeneity of the B_1^+ field is expected to decline with increasing B_0, thereby influencing the overall SNR gain. An experimental study investigating SNR dependency on B_0 in the human brain revealed that SNR $\propto B_0 1.65$ in the range of 3.0–9.4 T [109]. A recent simulation study also showed that SNR grows superlinearly with frequency, particularly in deeper regions of the sample; in less deep regions the SNR versus B_0 trend approached linearity [111].

An increase in magnetic field strength is particularly beneficial for X-nuclei imaging. An increase in B_0 from 9.4 to 21.1 T results in an SNR gain of ~3 compared to a gain of ~2 for ^{1}H MR [112]. We recently studied the influence of increasing B_0 on improving ^{19}F MR signal sensitivity [113]. Prior to the practical experiments, we estimated the expected SNR gain when moving from 9.4 to 21.1 T to be 2.7 [113]. We estimated SNR gain using the principle of reciprocity [110] and ignoring all flip angle, sequence and relaxation-dependent effects. The estimated SNR gain represents a baseline expectation, based on the information available for the specific hardware of each system. When introducing the relationship of the reference power for both MR systems, we estimated an SNR gain of ~3.8. In our practical experiments the ratio in SNR efficiency (SNR/$\sqrt{t}$ ratio) was estimated to be 7.29, when comparing the best possible conditions for both 21.1 and 9.4 T, and when including T_1 relaxation effects [113]. Differences between the actual SNR gains determined experimentally and those expected

from simulations are conceivable, due to minor inaccuracies in the assumptions made for the EMF simulations.

All research efforts ranging from new ^{19}F probe design, through optimization of ^{19}F MR data acquisition methods up to hardware developments hinge on the need for promoting ^{19}F MR signal in vivo, in order to answer crucial questions during pathology including kidney disease. Most of the efforts devoted to discovery and proof-of-principle research will benefit from an integration of all available tools and technologies, in order to reach the maximum potential for practical applications for patient health care.

Acknowledgments

This work was funded in part (Thoralf Niendorf, Sonia Waiczies, Andreas Pohlmann) by the German Research Foundation (Gefoerdert durch die Deutsche Forschungsgemeinschaft (DFG), Projektnummer 394046635, SFB 1365, RENOPROTECTION. Funded by the Deutsche Forschungsgemeinschaft (DFG, German Research Foundation), Project number 394046635, SFB 1365, RENOPROTECTION).

Also, our research is funded by the Deutsche Forschungsgemeinschaft to S.W. (DFG WA2804) and A.P. (DFG PO1869), by the European Research Council, ERC to T.N. (ThermalMR, EU project 743077), by the State of Florida and National Science Foundation Cooperative Agreement No. DMR-1157490 and DMR-1644779 to J.R. and the Visiting Scientist Program of the NHMFL to S.W. and H.W. (227000-110, Project 12643). We thank Professor Samuel Wickline from the University of South Florida for valuable feedback on the manuscript.

This publication is based upon work from COST Action PARENCHIMA, supported by European Cooperation in Science and Technology (COST). COST (www.cost.eu) is a funding agency for research and innovation networks. COST Actions help connect research initiatives across Europe and enable scientists to enrich their ideas by sharing them with their peers. This boosts their research, career, and innovation.

PARENCHIMA (renalmri.org) is a community-driven Action in the COST program of the European Union, which unites more than 200 experts in renal MRI from 30 countries with the aim to improve the reproducibility and standardization of renal MRI biomarkers.

References

1. Hingorani DV, Bernstein AS, Pagel MD (2015) A review of responsive MRI contrast agents: 2005–2014. Contrast Media Mol Imaging 10(4):245–265. https://doi.org/10.1002/cmmi.1629

2. Grenier N, Merville P, Combe C (2016) Radiologic imaging of the renal parenchyma structure and function. Nat Rev Nephrol 12 (6):348–359

3. Martinez GV, Zhang X, García-Martín ML, Morse DL, Woods M, Sherry AD, Gillies RJ (2011) Imaging the extracellular pH of tumors by MRI after injection of a single cocktail of T1 and T2 contrast agents. NMR Biomed 24(10):1380–1391. https://doi.org/10.1002/nbm.1701
4. Brooks RA, Brunetti A, Alger JR, Di Chiro G (1989) On the origin of paramagnetic inhomogeneity effects in blood. Magn Reson Med 12(2):241–248
5. Günther H (2013) NMR spectroscopy: basic principles, concepts and applications in chemistry. John Wiley & Sons, Hoboken, NJ
6. Dolbier WR (2009) Guide to fluorine NMR for organic chemists. John Wiley & Sons, Hoboken, NJ
7. Arami H, Khandhar A, Liggitt D, Krishnan KM (2015) In vivo delivery, pharmacokinetics, biodistribution and toxicity of iron oxide nanoparticles. Chem Soc Rev 44 (23):8576–8607. https://doi.org/10.1039/c5cs00541h
8. Toth GB, Varallyay CG, Horvath A, Bashir MR, Choyke PL, Daldrup-Link HE, Dosa E, Finn JP, Gahramanov S, Harisinghani M, Macdougall I, Neuwelt A, Vasanawala SS, Ambady P, Barajas R, Cetas JS, Ciporen J, DeLoughery TJ, Doolittle ND, Fu R, Grinstead J, Guimaraes AR, Hamilton BE, Li X, McConnell HL, Muldoon LL, Nesbit G, Netto JP, Petterson D, Rooney WD, Schwartz D, Szidonya L, Neuwelt EA (2017) Current and potential imaging applications of ferumoxytol for magnetic resonance imaging. Kidney Int 92(1):47–66. https://doi.org/10.1016/j.kint.2016.12.037
9. Feng Q, Liu Y, Huang J, Chen K, Huang J, Xiao K (2018) Uptake, distribution, clearance, and toxicity of iron oxide nanoparticles with different sizes and coatings. Sci Rep 8 (1):2082. https://doi.org/10.1038/s41598-018-19628-z
10. Longmire M, Choyke PL, Kobayashi H (2008) Clearance properties of nano-sized particles and molecules as imaging agents: considerations and caveats. Nanomedicine (Lond) 3(5):703–717. https://doi.org/10.2217/17435889.3.5.703
11. O'Connor PM (2006) Renal oxygen delivery: matching delivery to metabolic demand. Clin Exp Pharmacol Physiol 33(10):961–967. https://doi.org/10.1111/j.1440-1681.2006.04475.x
12. Hansell P, Welch WJ, Blantz RC, Palm F (2013) Determinants of kidney oxygen consumption and their relationship to tissue oxygen tension in diabetes and hypertension. Clin Exp Pharmacol Physiol 40(2):123–137. https://doi.org/10.1111/1440-1681.12034
13. Le Dorze M, Legrand M, Payen D, Ince C (2009) The role of the microcirculation in acute kidney injury. Curr Opin Crit Care 15 (6):503–508. https://doi.org/10.1097/MCC.0b013e328332f6cf
14. Ries M, Basseau F, Tyndal B, Jones R, Deminière C, Catargi B, Combe C, Moonen CWT, Grenier N (2003) Renal diffusion and BOLD MRI in experimental diabetic nephropathy. J Magn Reson Imaging 17 (1):104–113. https://doi.org/10.1002/jmri.10224
15. Prasad PV (2006) Evaluation of intra-renal oxygenation by BOLD MRI. Nephron Clin Pract 103(2):c58–c65. https://doi.org/10.1159/000090610
16. Niendorf T, Pohlmann A, Arakelyan K, Flemming B, Cantow K, Hentschel J, Grosenick D, Ladwig M, Reimann H, Klix S, Waiczies S, Seeliger E (2015) How bold is blood oxygenation level-dependent (BOLD) magnetic resonance imaging of the kidney? Opportunities, challenges and future directions. Acta Physiol 213(1):19–38. https://doi.org/10.1111/apha.12393
17. Dardzinski BJ, Sotak CH (1994) Rapid tissue oxygen tension mapping using 19F inversion-recovery echo-planar imaging of P erfluoro-15-crown-5-ether. Magn Reson Med 32 (1):88–97
18. Noth U, Morrissey SP, Deichmann R, Adolf H, Schwarzbauer C, Lutz J, Haase A (1995) In vivo measurement of partial oxygen pressure in large vessels and in the reticuloendothelial system using fast 19F-MRI. Magn Reson Med 34(5):738–745
19. Chen J, Vemuri C, Palekar RU, Gaut JP, Goette M, Hu L, Cui G, Zhang H, Wickline SA (2015) Antithrombin nanoparticles improve kidney reperfusion and protect kidney function after ischemia-reperfusion injury. Am J Physiol Renal Physiol 308(7):28
20. Hu L, Chen J, Yang X, Senpan A, Allen JS, Yanaba N, Caruthers SD, Lanza GM, Hammerman MR, Wickline SA (2013) Assessing intrarenal nonperfusion and vascular leakage in acute kidney injury with multinuclear 1H/19F MRI and perfluorocarbon nanoparticles. Magn Reson Med. https://doi.org/10.1002/mrm.24851
21. Riess JG (2005) Understanding the fundamentals of perfluorocarbons and perfluorocarbon emulsions relevant to in vivo oxygen

delivery. Artif Cell Blood Sub Biotechnol 33 (1):47–63

22. Schmieder AH, Caruthers SD, Keupp J, Wickline SA, Lanza GM (2015) Recent advances in (19)fluorine magnetic resonance imaging with perfluorocarbon emulsions. Engineering (Beijing, China) 1(4):475–489. https://doi.org/10.15302/j-eng-2015103
23. Mitsuno T, Ohyanagi H, Naito R (1982) Clinical studies of a perfluorochemical whole blood substitute (Fluosol-DA) summary of 186 cases. Ann Surg 195(1):60–69. https://doi.org/10.1097/00000658-198201001-00010
24. Gould SA, Rosen AL, Sehgal LR, Sehgal HL, Langdale LA, Krause LM, Rice CL, Chamberlin WH, Moss GS (1986) Fluosol-DA as a red-cell substitute in acute anemia. N Engl J Med 314(26):1653–1656. https://doi.org/10.1056/nejm198606263142601
25. McFarland E, Koutcher JA, Rosen BR, Teicher B, Brady TJ (1985) In vivo 19F NMR imaging. J Comput Assist Tomogr 9 (1):8–15
26. Jacoby C, Temme S, Mayenfels F, Benoit N, Krafft MP, Schubert R, Schrader J, Flögel U (2014) Probing different perfluorocarbons for in vivo inflammation imaging by 19F MRI: image reconstruction, biological half-lives and sensitivity. NMR Biomed 27 (3):261–271. https://doi.org/10.1002/nbm.3059
27. Parhami P, Fung B (1983) Fluorine-19 relaxation study of perfluoro chemicals as oxygen carriers. J Phys Chem 87(11):1928–1931
28. Mason RP, Nunnally RL, Antich PP (1991) Tissue oxygenation: a novel determination using 19F surface coil NMR spectroscopy of sequestered perfluorocarbon emulsion. Magn Reson Med 18(1):71–79. https://doi.org/10.1002/mrm.1910180109
29. Mason RP, Jeffrey FMH, Malloy CR, Babcock EE, Antich PP (1992) A noninvasive assessment of myocardial oxygen tension: 19f nmr spectroscopy of sequestered perfluorocarbon emulsion. Magn Reson Med 27(2):310–317. https://doi.org/10.1002/mrm.1910270210
30. Pereira PCB, Miranda DM, Oliveira EA, Silva ACSE (2009) Molecular pathophysiology of renal tubular acidosis. Curr Genomics 10 (1):51–59. https://doi.org/10.2174/138920209787581262
31. Zhang S, Wu K, Sherry AD (1999) A novel pH-sensitive MRI contrast agent. Angew Chem Int Ed 38(21):3192–3194. https://doi.org/10.1002/(sici)1521-3773(19991102)38:21<3192::aid-anie3192>3.0.co;2-#
32. Longo DL, Busato A, Lanzardo S, Antico F, Aime S (2013) Imaging the pH evolution of an acute kidney injury model by means of iopamidol, a MRI-CEST pH-responsive contrast agent. Magn Reson Med 70 (3):859–864. https://doi.org/10.1002/mrm.24513
33. Raghunand N, Gatenby RA, Gillies RJ (2003) Microenvironmental and cellular consequences of altered blood flow in tumours. Br J Radiol 76(Suppl_1):S11–S22. https://doi.org/10.1259/bjr/12913493
34. Gianolio E, Napolitano R, Fedeli F, Arena F, Aime S (2009) Poly-β-cyclodextrin based platform for pH mapping via a ratiometric 19F/1H MRI method. Chem Commun 40:6044–6046. https://doi.org/10.1039/B914540K
35. Chang YC, Graves DJ (1985) Use of 6-fluoroderivatives of pyridoxal and pyridoxal phosphate in the study of the coenzyme function in glycogen phosphorylase. J Biol Chem 260(5):2709–2714
36. Mehta VD, Kulkarni PV, Mason RP, Constantinescu A, Aravind S, Goomer N, Antich PP (1994) 6-Fluoropyridoxol: a novel probe of cellular pH using 19F NMR spectroscopy. FEBS Lett 349(2):234–238. https://doi.org/10.1016/0014-5793(94)00675-x
37. He S, Mason RP, Hunjan S, Mehta VD, Arora V, Katipally R, Kulkarni PV, Antich PP (1998) Development of novel 19F NMR pH indicators: synthesis and evaluation of a series of fluorinated vitamin B6 analogues. Bioorg Med Chem 6(9):1631–1639. https://doi.org/10.1016/S0968-0896(98)00104-7
38. Neubauer AM, Myerson J, Caruthers SD, Hockett FD, Winter PM, Chen J, Gaffney PJ, Robertson JD, Lanza GM, Wickline SA (2008) Gadolinium-modulated 19F signals from perfluorocarbon nanoparticles as a new strategy for molecular imaging. Magn Reson Med 60(5):1066–1072
39. Chalmers KH, De Luca E, Hogg NHM, Kenwright AM, Kuprov I, Parker D, Botta M, Wilson JI, Blamire AM (2010) Design principles and theory of paramagnetic fluorine-labelled lanthanide complexes as probes for 19F magnetic resonance: a proof-of-concept study. Chem Eur J 16(1):134–148. https://doi.org/10.1002/chem.200902300
40. Gaudette AI, Thorarinsdottir AE, Harris TD (2017) pH-dependent spin state population and 19F NMR chemical shift via remote ligand protonation in an iron(ii) complex.

Chem Commun 53(96):12962–12965. https://doi.org/10.1039/C7CC08158H

41. Xie D, Ohman LE, Que EL (2018) Towards Ni(II) complexes with spin switches for 19F MR-based pH sensing. MAGMA. https://doi.org/10.1007/s10334-018-0698-4
42. Preslar AT, Tantakitti F, Park K, Zhang S, Stupp SI, Meade TJ (2016) 19F magnetic resonance imaging signals from peptide amphiphile nanostructures are strongly affected by their shape. ACS Nano 10 (8):7376–7384. https://doi.org/10.1021/acsnano.6b00267
43. Liu KD, Glidden DV, Eisner MD, Parsons PE, Ware LB, Wheeler A, Korpak A, Thompson BT, Chertow GM, Matthay MA (2007) Predictive and pathogenetic value of plasma biomarkers for acute kidney injury in patients with acute lung injury. Crit Care Med 35 (12):2755–2761
44. Levy EM, Viscoli CM, Horwitz RI (1996) The effect of acute renal failure on mortality. A cohort analysis. JAMA 275 (19):1489–1494
45. Jorres A, Gahl GM, Dobis C, Polenakovic MH, Cakalaroski K, Rutkowski B, Kisielnicka E, Krieter DH, Rumpf KW, Guenther C, Gaus W, Hoegel J (1999) Haemodialysis-membrane biocompatibility and mortality of patients with dialysis-dependent acute renal failure: a prospective randomised multicentre trial. International Multicentre Study Group. Lancet 354 (9187):1337–1341
46. Brouns R, De Deyn PP (2004) Neurological complications in renal failure: a review. Clin Neurol Neurosurg 107(1):1–16. https://doi.org/10.1016/j.clineuro.2004.07.012
47. Flögel U, Ding Z, Hardung H, Jander S, Reichmann G, Jacoby C, Schubert R, Schrader J (2008) In vivo monitoring of inflammation after cardiac and cerebral ischemia by fluorine magnetic resonance imaging. Circulation 118(2):140–148
48. Hitchens TK, Ye Q, Eytan DF, Janjic JM, Ahrens ET, Ho C (2011) 19F MRI detection of acute allograft rejection with in vivo perfluorocarbon labeling of immune cells. Magn Reson Med 65(4):1144–1153. https://doi.org/10.1002/mrm.22702
49. Temme S, Bonner F, Schrader J, Flögel U (2012) 19F magnetic resonance imaging of endogenous macrophages in inflammation. Wiley Interdiscip Rev Nanomed Nanobiotechnol 4(3):329–343. https://doi.org/10.1002/wnan.1163
50. Waiczies H, Lepore S, Drechsler S, Qadri F, Purfurst B, Sydow K, Dathe M, Kuhne A, Lindel T, Hoffmann W, Pohlmann A, Niendorf T, Waiczies S (2013) Visualizing brain inflammation with a shingled-leg radiofrequency head probe for 19F/1H MRI. Sci Rep 3:1280. https://doi.org/10.1038/srep01280
51. Flögel U, Burghoff S, van Lent PL, Temme S, Galbarz L, Ding Z, El-Tayeb A, Huels S, Bonner F, Borg N, Jacoby C, Muller CE, van den Berg WB, Schrader J (2012) Selective activation of adenosine A2A receptors on immune cells by a CD73-dependent prodrug suppresses joint inflammation in experimental rheumatoid arthritis. Sci Transl Med 4 (146):146ra108. https://doi.org/10.1126/scitranslmed.3003717
52. Ahrens ET, Flores R, Xu H, Morel PA (2005) In vivo imaging platform for tracking immunotherapeutic cells. Nat Biotechnol 23 (8):983–987
53. Waiczies H, Lepore S, Janitzek N, Hagen U, Seifert F, Ittermann B, Purfurst B, Pezzutto A, Paul F, Niendorf T, Waiczies S (2011) Perfluorocarbon particle size influences magnetic resonance signal and immunological properties of dendritic cells. PLoS One 6(7):e21981
54. Waiczies H, Guenther M, Skodowski J, Lepore S, Pohlmann A, Niendorf T, Waiczies S (2013) Monitoring dendritic cell migration using 19F/1H magnetic resonance imaging. J Vis Exp 73:e50251. https://doi.org/10.3791/50251
55. Ahrens ET, Helfer BM, O'Hanlon CF, Schirda C (2014) Clinical cell therapy imaging using a perfluorocarbon tracer and fluorine-19 MRI. Magn Reson Med 72 (6):1696-1701. https://doi.org/10.1002/mrm.25454
56. Ten Brinke A, Hilkens CMU, Cools N, Geissler EK, Hutchinson JA, Lombardi G, Lord P, Sawitzki B, Trzonkowski P, Van Ham SM, Martinez-Caceres EM (2015) Clinical use of tolerogenic dendritic cells-harmonization approach in european collaborative effort. Mediat Inflamm 2015:8. https://doi.org/10.1155/2015/471719
57. Hutchinson JA, Riquelme P, Sawitzki B, Tomiuk S, Miqueu P, Zuhayra M, Oberg HH, Pascher A, Lützen U, Janßen U, Broichhausen C, Renders L, Thaiss F, Scheuermann E, Henze E, Volk H-D, Chatenoud L, Lechler RI, Wood KJ, Kabelitz D, Schlitt HJ, Geissler EK, Fändrich F (2011) Cutting edge: immunological consequences and trafficking of human regulatory

macrophages administered to renal transplant recipients. J Immunol 187(5):2072–2078. https://doi.org/10.4049/jimmunol.1100762

58. Ruiz-Cabello J, Barnett BP, Bottomley PA, Bulte JW (2011) Fluorine (19F) MRS and MRI in biomedicine. NMR Biomed 24 (2):114–129. https://doi.org/10.1002/nbm.1570
59. Jirak D, Galisova A, Kolouchova K, Babuka D, Hruby M (2018) Fluorine polymer probes for magnetic resonance imaging: quo vadis? MAGMA. https://doi.org/10.1007/s10334-018-0724-6
60. Helfer BM, Balducci A, Nelson AD, Janjic JM, Gil RR, Kalinski P, de Vries IJ, Ahrens ET, Mailliard RB (2010) Functional assessment of human dendritic cells labeled for in vivo (19)F magnetic resonance imaging cell tracking. Cytotherapy 12(2):238–250. https://doi.org/10.3109/14653240903446902
61. Bonetto F, Srinivas M, Heerschap A, Mailliard R, Ahrens ET, Figdor CG, de Vries IJ (2011) A novel (19)F agent for detection and quantification of human dendritic cells using magnetic resonance imaging. Int J Cancer 129(2):365–373. https://doi.org/10.1002/ijc.25672
62. Waiczies S, Lepore S, Sydow K, Drechsler S, Ku MC, Martin C, Lorenz D, Schutz I, Reimann HM, Purfurst B, Dieringer MA, Waiczies H, Dathe M, Pohlmann A, Niendorf T (2015) Anchoring dipalmitoyl phosphoethanolamine to nanoparticles boosts cellular uptake and fluorine-19 magnetic resonance signal. Sci Rep 5:8427. https://doi.org/10.1038/srep08427
63. Hutchinson JA, Ahrens N, Riquelme P, Walter L, Gruber M, Böger CA, Farkas S, Scherer MN, Broichhausen C, Bein T, Schlitt H-J, Fändrich F, Banas B, Geissler EK (2014) Clinical management of patients receiving cell-based immunoregulatory therapy. Transfusion 54(9):2336–2343. https://doi.org/10.1111/trf.12641
64. Bagalkot V, Deiuliis JA, Rajagopalan S, Maiseyeu A (2016) "Eat me" imaging and therapy. Adv Drug Deliv Rev 99(Pt A):2–11. https://doi.org/10.1016/j.addr.2016.01.009
65. Lindner JR, Song J, Xu F, Klibanov AL, Singbartl K, Ley K, Kaul S (2000) Noninvasive ultrasound imaging of inflammation using microbubbles targeted to activated leukocytes. Inflammation 102:2745–2750
66. Steinman RM, Mellman IS, Muller WA, Cohn ZA (1983) Endocytosis and the recycling of plasma membrane. J Cell Biol 96(1):1–27
67. Kaneda MM, Sasaki Y, Lanza GM, Milbrandt J, Wickline SA (2010) Mechanisms of nucleotide trafficking during siRNA delivery to endothelial cells using perfluorocarbon nanoemulsions. Biomaterials 31 (11):3079–3086
68. Partlow KC, Lanza GM, Wickline SA (2008) Exploiting lipid raft transport with membrane targeted nanoparticles: a strategy for cytosolic drug delivery. Biomaterials 29 (23):3367–3375
69. Chapelin F, Capitini CM, Ahrens ET (2018) Fluorine-19 MRI for detection and quantification of immune cell therapy for cancer. J Immunother Cancer 6(1):105. https://doi.org/10.1186/s40425-018-0416-9
70. Chapelin F, Gao S, Okada H, Weber TG, Messer K, Ahrens ET (2017) Fluorine-19 nuclear magnetic resonance of chimeric antigen receptor T cell biodistribution in murine cancer model. Sci Rep 7(1):17748. https://doi.org/10.1038/s41598-017-17669-4
71. Sanz-Ortega L, Rojas JM, Marcos A, Portilla Y, Stein JV, Barber DF (2019) T cells loaded with magnetic nanoparticles are retained in peripheral lymph nodes by the application of a magnetic field. J Nanobiotechnol 17(1):14. https://doi.org/10.1186/s12951-019-0440-z
72. Stephens DJ, Allan VJ (2003) Light microscopy techniques for live cell imaging. Science 300(5616):82–86. https://doi.org/10.1126/science.1082160
73. Bouvain P, Flocke V, Krämer W, Schubert R, Schrader J, Flögel U, Temme S (2018) Dissociation of 19F and fluorescence signal upon cellular uptake of dual-contrast perfluorocarbon nanoemulsions. MAGMA. https://doi.org/10.1007/s10334-018-0723-7
74. Gustafson HH, Holt-Casper D, Grainger DW, Ghandehari H (2015) Nanoparticle uptake: the phagocyte problem. Nano Today 10(4):487–510. https://doi.org/10.1016/j.nantod.2015.06.006
75. Waiczies S, Niendorf T, Lombardi G (2017) Labeling of cell therapies: how can we get it right? Oncoimmunology 2017:e1345403. https://doi.org/10.1080/2162402x.2017.1345403
76. Tirotta I, Dichiarante V, Pigliacelli C, Cavallo G, Terraneo G, Bombelli FB, Metrangolo P, Resnati G (2015) 19F magnetic resonance imaging (MRI): from design of materials to clinical applications. Chem Rev 115(2):1106–1129. https://doi.org/10.1021/cr500286d
77. Jiang ZX, Liu X, Jeong EK, Yu YB (2009) Symmetry-guided design and fluorous synthesis of a stable and rapidly excreted imaging

tracer for 19F MRI. Angew Chem Int Edn 48 (26):4755–4758. https://doi.org/10.1002/anie.200901005

78. Tirotta I, Mastropietro A, Cordiglieri C, Gazzera L, Baggi F, Baselli G, Bruzzone MG, Zucca I, Cavallo G, Terraneo G, Baldelli Bombelli F, Metrangolo P, Resnati G (2014) A superfluorinated molecular probe for highly sensitive in vivo(19)F-MRI. J Am Chem Soc 136(24):8524–8527. https://doi.org/10.1021/ja503270n
79. Peterson KL, Srivastava K, Pierre VC (2018) Fluorinated paramagnetic complexes: sensitive and responsive probes for magnetic resonance spectroscopy and imaging. Front Chem 6:160–160. https://doi.org/10.3389/fchem.2018.00160
80. Kislukhin AA, Xu H, Adams SR, Narsinh KH, Tsien RY, Ahrens ET (2016) Paramagnetic fluorinated nanoemulsions for sensitive cellular fluorine-19 magnetic resonance imaging. Nat Mater 15:662. https://doi.org/10.1038/nmat4585. https://www.nature.com/articles/nmat4585#supplementary-information
81. Harvey P, Kuprov I, Parker D (2012) Lanthanide complexes as paramagnetic probes for 19F magnetic resonance. Eur J Inorg Chem 2012(12):2015–2022
82. Jiang Z-X, Feng Y, Yu YB (2011) Fluorinated paramagnetic chelates as potential multichromic 19 F tracer agents. Chem Commun 47(25):7233–7235
83. Hu L, Zhang L, Chen J, Lanza GM, Wickline SA (2011) Diffusional mechanisms augment the fluorine MR relaxation in paramagnetic perfluorocarbon nanoparticles that provides a “relaxation switch” for detecting cellular endosomal activation. J Magn Reson Imaging 34(3):653–661
84. Srivastava K, Ferrauto G, Young VG, Aime S, Pierre VC (2017) Eight-coordinate, stable Fe (II) complex as a dual 19F and CEST contrast agent for ratiometric pH imaging. Inorg Chem 56(20):12206–12213. https://doi.org/10.1021/acs.inorgchem.7b01629
85. Yu M, Bouley BS, Xie D, Que EL (2019) Highly fluorinated metal complexes as dual 19F and PARACEST imaging agents. Dalton Trans. https://doi.org/10.1039/C9DT01852B
86. Faber C, Schmid F (2016) Pulse sequence considerations and schemes. Fluorine magnetic resonance imaging. Pan Stanford Publishing, Singapore, pp 1–28
87. Chalmers KH, Kenwright AM, Parker D, Blamire AM (2011) 19F-lanthanide complexes with increased sensitivity for 19F-MRI: optimization of the MR acquisition. Magn Reson Med 66(4):931–936. https://doi.org/10.1002/mrm.22881
88. Schmid F, Höltke C, Parker D, Faber C (2013) Boosting 19F MRI—SNR efficient detection of paramagnetic contrast agents using ultrafast sequences. Magn Reson Med 69(4):1056–1062. https://doi.org/10.1002/mrm.24341
89. Goette MJ, Keupp J, Rahmer J, Lanza GM, Wickline SA, Caruthers SD (2015) Balanced UTE-SSFP for 19F MR imaging of complex spectra. Magn Reson Med 74(2):537–543. https://doi.org/10.1002/mrm.25437
90. Mastropietro A, De Bernardi E, Breschi GL, Zucca I, Cametti M, Soffientini CD, de Curtis M, Terraneo G, Metrangolo P, Spreafico R, Resnati G, Baselli G (2014) Optimization of rapid acquisition with relaxation enhancement (RARE) pulse sequence parameters for (1)(9)F-MRI studies. J Magn Reson Imaging 40(1):162–170
91. Srinivas M, Morel PA, Ernst LA, Laidlaw DH, Ahrens ET (2007) Fluorine-19 MRI for visualization and quantification of cell migration in a diabetes model. Magn Reson Med 58 (4):725–734. https://doi.org/10.1002/mrm.21352
92. Hennig J, Nauerth A, Friedburg H (1986) RARE imaging: a fast imaging method for clinical MR. Magn Reson Med 3:823–833. https://doi.org/10.1002/mrm.1910030602
93. Rahmer J, Börnert P, Groen J, Bos C (2006) Three-dimensional radial ultrashort echo-time imaging with T2 adapted sampling. Magn Reson Med 55(5):1075–1082. https://doi.org/10.1002/mrm.20868
94. Hennig J (1999) K-space sampling strategies. Eur Radiol 9(6):1020–1031. https://doi.org/10.1007/s003300050788
95. Keupp J, Rahmer J, Grässlin I, Mazurkewitz PC, Schaeffter T, Lanza GM, Wickline SA, Caruthers SD (2011) Simultaneous dual-nuclei imaging for motion corrected detection and quantification of 19F imaging agents. Magn Reson Med 66(4):1116–1122. https://doi.org/10.1002/mrm.22877
96. Hu L, Hockett FD, Chen J, Zhang L, Caruthers SD, Lanza GM, Wickline SA (2011) A generalized strategy for designing (19)F/(1)H dual-frequency MRI coil for small animal imaging at 4.7 Tesla. J Magn Reson Imaging 34(1):245–252
97. Hoult DI, Richards RE (1976) The signal-to-noise ratio of the nuclear magnetic resonance experiment. J Magn Reson 24(1):71–85
98. Kovacs H, Moskau D, Spraul M (2005) Cryogenically cooled probes – a leap in NMR

technology. Prog Nucl Magn Reson Spectrosc 46(2–3):131–155

99. Baltes C, Radzwill N, Bosshard S, Marek D, Rudin M (2009) Micro MRI of the mouse brain using a novel 400 MHz cryogenic quadrature RF probe. NMR Biomed 22 (8):834–842
100. Waiczies S, Millward JM, Starke L, Delgado PR, Huelnhagen T, Prinz C, Marek D, Wecker D, Wissmann R, Koch SP, Boehm-Sturm P, Waiczies H, Niendorf T, Pohlmann A (2017) Enhanced fluorine-19 MRI sensitivity using a cryogenic radiofrequency probe: technical developments and ex vivo demonstration in a mouse model of neuroinflammation. Sci Rep 7(1):9808. https://doi.org/10.1038/s41598-017-09622-2
101. Sack M, Wetterling F, Sartorius A, Ende G, Weber-Fahr W (2014) Signal-to-noise ratio of a mouse brain 13C CryoProbe™ system in comparison with room temperature coils: spectroscopic phantom and in vivo results. NMR Biomed 27(6):709–715. https://doi.org/10.1002/nbm.3110
102. Axel L, Hayes C (1985) Surface coil magnetic resonance imaging. Arch Int Physiol Biochim 93(5):11–18. https://doi.org/10.3109/13813458509080620
103. Crowley MG, Evelhoch JL, JJH A (1985) The surface-coil NMR receiver in the presence of homogeneous B1 excitation. J Magn Reson 64(1):20–31. https://doi.org/10.1016/0022-2364(85)90026-5
104. Goette MJ, Lanza GM, Caruthers SD, Wickline SA (2015) Improved quantitative (19) F MR molecular imaging with flip angle calibration and B1 -mapping compensation. J Magn Reson Imaging 42(2):488–494. https://doi.org/10.1002/jmri.24812
105. Vernikouskaya I, Pochert A, Lindén M, Rasche V (2018) Quantitative 19F MRI of perfluoro-15-crown-5-ether using uniformity correction of the spin excitation and signal reception. MAGMA. https://doi.org/10.1007/s10334-018-0696-6
106. Ladd ME (2018) The quest for higher sensitivity in MRI through higher magnetic fields. Z Med Phys 28(1):1–3. https://doi.org/10.1016/j.zemedi.2017.12.001
107. Niendorf T, Barth M, Kober F, Trattnig S (2016) From ultrahigh to extreme field magnetic resonance: where physics, biology and medicine meet. Magma (New York, NY) 29 (3):309–311. https://doi.org/10.1007/s10334-016-0564-1
108. Hoult DI, Lauterbur PC (1979) Sensitivity of the zeugmatographic experiment involving human samples. J Magn Reson 34 (2):425–433
109. Pohmann R, Speck O, Scheffler K (2016) Signal-to-noise ratio and MR tissue parameters in human brain imaging at 3, 7, and 9.4 tesla using current receive coil arrays. Magn Reson Med 75(2):801–809. https://doi.org/10.1002/mrm.25677
110. Hoult DI (2000) The principle of reciprocity in signal strength calculations—a mathematical guide. Concept Magn Reson 12 (4):173–187. https://doi.org/10.1002/1099-0534(2000)12:4<173::AID-CMR1>3.0.CO;2-Q
111. Guérin B, Villena JF, Polimeridis AG, Adalsteinsson E, Daniel L, White JK, Wald LL (2017) The ultimate signal-to-noise ratio in realistic body models. Magn Reson Med 78 (5):1969–1980. https://doi.org/10.1002/mrm.26564
112. Schepkin VD, Brey WW, Gor'kov PL, Grant SC (2010) Initial in vivo rodent sodium and proton MR imaging at 21.1 T. Magn Reson Imaging 28(3):400–407. https://doi.org/10.1016/j.mri.2009.10.002
113. Waiczies S, Rosenberg JT, Prinz C, Starke L, Millward JM, Ramos Delgado P, Pohlmann A, Kühne A, Waiczies H, Niendorf T (2018) Fluorine-19 magnetic resonance at 21.1 Tesla to detect brain inflammation. Proc Intl Soc Mag Reson Med 26:3314